AGU PUBLICATIONS

JGR

Journal of Geophysical Research: Oceans

RESEARCH ARTICLE

10.1002/2014JC010286

ENSO-driven interhemispheric Pacific mass transports

Shayne McGregor[1,2], Paul Spence[1,2], Franziska U. Schwarzkopf[3], Matthew H. England[1,2], Agus Santoso[1,2], William S. Kessler[4], Axel Timmermann[5], and Claus W. Böning[3]

[1]Climate Change Research Centre, University of New South Wales, Sydney, New South Wales, Australia, [2]ARC Centre of Excellence for Climate System Science, University of New South Wales, Sydney, New South Wales, Australia, [3]GEOMAR Helmholtz Centre for Ocean Research, Kiel, Germany, [4]NOAA/PMEL, Seattle, Washington, USA, [5]International Pacific Research Center and Department of Oceanography, SOEST, University of Hawaii, Honolulu, Hawaii, USA

Key Points:
- ENSO's southward wind shift is mostly responsible for interhemispheric exchanges
- ENSO phase asymmetry in the magnitude of the interhemispheric exchange
- El Nino discharge is meridionally asymmetric while La Nina recharge is symmetric

Correspondence to:
S. McGregor,
shayne.mcgregor@unsw.edu.au

Citation:
McGregor, S., P. Spence, F. U. Schwarzkopf, M. H. England, A. Santoso, W. S. Kessler, A. Timmermann, and C. W. Böning (2014), ENSO-driven interhemispheric Pacific mass transports, *J. Geophys. Res. Oceans*, *119*, 6221–6237, doi:10.1002/2014JC010286.

Received 3 JUL 2014
Accepted 20 AUG 2014
Accepted article online 26 AUG 2014
Published online 17 SEP 2014

Abstract Previous studies have shown that ENSO's anomalous equatorial winds, including the observed southward shift of zonal winds that occurs around the event peak, can be reconstructed with the first two Empirical Orthogonal Functions (EOFs) of equatorial region wind stresses. Using a high-resolution ocean general circulation model, we investigate the effect of these two EOFs on changes in warm water volume (WWV), interhemispheric mass transports, and Indonesian Throughflow (ITF). Wind stress anomalies associated with the first EOF produce changes in WWV that are dynamically consistent with the conceptual recharge oscillator paradigm. The ITF is found to heavily damp these WWV changes, reducing their variance by half. Wind stress anomalies associated with the second EOF, which depicts the southward wind shift, are responsible for WWV changes that are of comparable magnitude to those driven by the first mode. The southward wind shift is also responsible for the majority of the observed interhemispheric upper ocean mass exchanges. These winds transfer mass between the Northern and the Southern Hemisphere during El Niño events. Whilst water is transferred in the opposite direction during La Niña events, the magnitude of this exchange is roughly half of that seen during El Niño events. Thus, the discharging of WWV during El Niño events is meridionally asymmetric, while the WWV recharging during a La Niña event is largely symmetric. The inclusion of the southward wind shift is also shown to allow ENSO to exchange mass with much higher latitudes than that allowed by the first EOF alone.

1. Introduction

Our understanding of the dynamics of the Earth's largest source of interannual climate variability, the El Niño-Southern Oscillation (ENSO), has significantly increased over the last three decades [*McPhaden et al*., 2006; *Chang et al*., 2006], with the success of theories such as the Recharge/Discharge Oscillator (RDO) [*Jin*, 1997]. The RDO theory highlights mass exchanges between the equatorial and off-equatorial regions in order to explain the phase transitions of ENSO. For instance, the poleward transport of equatorial region warm upper waters during El Niño events discharges Warm Water Volume (WWV) from the equatorial region, setting up conditions that tend to terminate the warm event. The basic principles of the RDO theory have been substantiated through the observational analyses of *Meinen and McPhaden* [2000]. It has been suggested that the discharge (recharge) during El Niño (La Niña) events occurs most prominently in the ocean interior [*Meinen and McPhaden*, 2001], with the Indonesian Throughflow (ITF) transport taking part in this recharge/discharge of heat [e.g., *Cai et al*., 2005].

While assuming that El Niño and La Niña events are mirror images of each other, the original RDO theory also assumes that the associated mass transports in the Northern Hemisphere (NH) mirror those of the Southern Hemisphere (SH). Observations, however, show an asymmetry in spatial structure and duration of opposing ENSO phases [e.g., *Okumura and Deser*, 2010], as well as a pronounced asymmetry in which the associated mass exchange prominently occurs in the NH and is nearly zero in the SH [*Kug et al*., 2003]. This hemispheric mass transport asymmetry is supported by the apparent meridional asymmetry associated with the Pacific Ocean's "recharge" mode (defined as the second Empirical Orthogonal Function (EOF) of 20°C isotherm depth) [*Meinen and McPhaden*, 2000].

The results of *Kug et al*. [2003] suggest that this meridional mass transport asymmetry is due to the meridionally asymmetric distribution of the wind anomalies that are linearly related to ENSO (which is represented

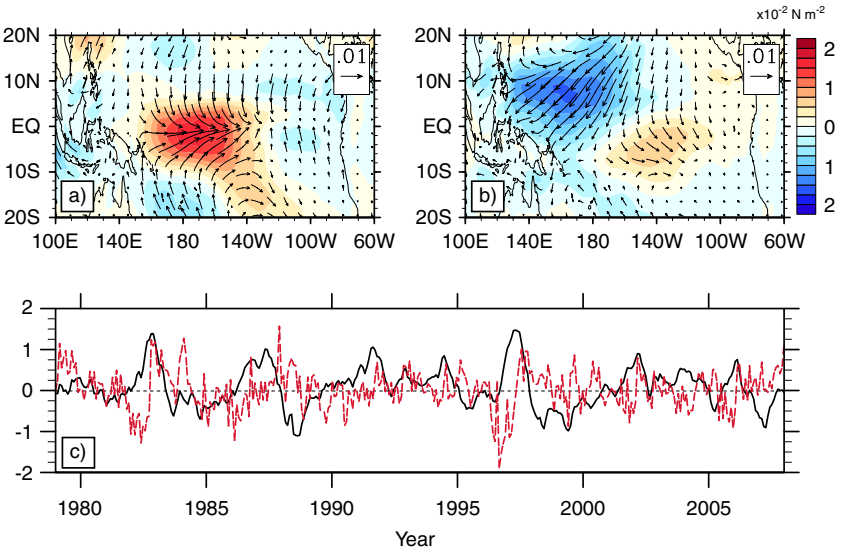

Figure 1. Wind stress (N m^{-2}) patterns (a) linearly related to ENSO (Niño 3.4 region SSTA) (also referred to as τ_{sym}, see section 3), and (b) of the second EOF of equatorial region wind stresses (also referred to as τ_{asym}, see section 3). The zonal component is shaded. (c) Time evolution for ENSO (Niño 3.4 region SSTA, or τ_{sym}) shown in black and τ_{asym} shown in red.

by the NINO3.4 index, SSTA averaged in the region 5°N–5°S, 90°W–150°W). Despite being broadly symmetric about the equator, the spatial pattern of the regressed wind stresses onto NINO3.4 does display stronger zonal wind speeds south of the equator (Figure 1a). This regression pattern is very similar to the first EOF of wind stress anomalies in the equatorial region (not shown).

It has recently been noted by *McGregor et al*. [2012a] that the meridional asymmetry of the Pacific Ocean's "recharge" mode is related to the second EOF of equatorial wind stress anomalies (Figure 1b). This second EOF displays a Philippine Sea anticyclone-type structure [*Wang et al*., 1999] in the north-west tropical Pacific (Figure 1b). Taken with its accompanying principal component time series (Figure 1c), the north-west tropical Pacific winds associated with this EOF should display a cyclonic circulation prior to the peak of El Niño events, which then abruptly changes to an anticyclonic circulation around the peak of the event.

Idealized atmospheric General Circulation Model (GCM) experiments and spectral analysis show that this second EOF of equatorial wind stress anomalies is representative of a physically meaningful mode that is generated in response to nonlinear interaction between ENSO and the annual cycle [*Stuecker et al*., 2013]. Reconstructing near-equatorial wind stress anomalies with these first two EOFs reveals that the linear combination of these two spatial patterns allows the wind stress anomalies during ENSO events to shift southward around the peak of the event. This southward wind shift is consistent with observations [e.g., *Harrison*, 1987], and it ultimately allows the wind stress anomalies associated with ENSO to become more meridionally asymmetric in the months after the event peak [*McGregor et al*., 2012a]. Thus, the meridional wind shift represented by the second EOF could potentially influence meridional ocean mass transports during ENSO events. This factor was not considered by *Kug et al*. [2003] as it has only recently been identified and related to ENSO [*McGregor et al*., 2012a, 2013; *Stuecker et al*., 2013]; however, it is notable that the *Kug et al*. [2003] study highlighted the role of meridional asymmetries the wind stress anomalies that are linearly related to ENSO.

Further, the meridional wind movement produced by wind stresses reconstructed with EOF1 and EOF2 increases with increasing El Niño amplitude, while remaining relatively small regardless of La Niña amplitude [*McGregor et al*., 2013]. This nonlinearity is consistent with the sea level studies of *Alory and Delcroix* [2002] and *Widlansky et al*. [2014], who showed that the meridional asymmetry of ENSO's recharge/discharge mode is most pronounced during strong El Niño events. This observation implies that while the discharge of heat during an El Niño event may be asymmetric and the asymmetry may increase with increasing event magnitude, the recharge of heat during La Niña events may be largely symmetric.

In this study, we investigate the effect of the equatorial wind stress anomalies described by the first two EOFs on the WWV changes and interhemispheric mass transport asymmetry seen during ENSO events using a high-resolution Ocean General Circulation model (OGCM). The model is shown here to realistically represent the jets traveling through the complex bathymetry of the western Pacific and more accurate pathways for waters feeding the Equatorial Under Current (EUC). We then seek to detail the ENSO phase (El Niño-La Niña event) asymmetries seen in these transports. The manuscript is laid out as follows. Section 2 details the observational data sets and OGCM utilized in this study, while section 3 details the numerous OGCM simulations carried out. The results of the OGCM simulations are presented in section 4 where the transports, changes in equatorial region warm water volume (WWV), interhemispheric exchanges, and Indonesian Throughflow (ITF) are highlighted. Section 5 discusses the implications and conclusions.

2. Data and Model Details

2.1. Wind Stress Anomalies

Monthly mean wind data from the ECMWF interim reanalysis (ERA-interim) products are utilized here spanning the period 1979–2011 [*Dee and Uppala*, 2009]. This reanalysis product has been shown to reproduce the tropical Pacific Ocean's observed interannual sea surface height variability with reasonable fidelity [*McGregor et al*., 2012b]. Surface winds were converted to wind stress anomalies using the quadratic stress law: $(\tau_x, \tau_y) = C_d\ \rho_a$ (U,V) W, where U, V are the zonal and meridional surface wind velocities, respectively, W is the surface wind speed, $\rho_a = 1.2$ kg m^{-3} is a reference atmospheric density, and $C_d = 1.5e^{-3}$ is the dimensionless drag coefficient. Anomalies of wind stress are computed relative to a mean seasonal cycle based on the 1979–2011 climatology.

2.2. Sea Surface Temperatures

The monthly anomalies of the NINO3.4 index (N34) utilized in this study are derived from NOAAs Extended Reconstruction Sea Surface Temperature (ERSST) version 3b [*Smith et al*., 2008]. Note that the N34 anomalies are computed relative to a mean seasonal cycle based on the 1971–2000 climatology.

2.3. Ocean General Circulation Model (OGCM)

The Ocean GCM (OGCM) we utilize here is a high-resolution nested model of the Tropical Pacific (TROPAC01). This model is built on the Nucleus for European Modeling of the Ocean (NEMO) version 3.1.1 code [*Madec*, 2008] in the Drakkar configuration using a tripolar, curvilinear grid. The global model has a nominal 0.5° horizontal resolution (ORCA05) and 46 vertical levels. It is a primitive equation ocean-sea ice model, forced by prescribed atmospheric conditions. The hydrodynamic equations are discretized on a staggered Arakawa-C grid [*Arakawa and Lamb*, 1977] with a free sea surface; a preconditioned conjugate gradient solver is used.

A high-resolution 0.1° "nest" of the Tropical Pacific spanning the area from 73°E to 63°W and 49°S to 31°N is embedded into the global model. This includes the Indonesian passages, the Solomon Sea and its complex straits, the complex Mindanao coast, and Australia. The regional refinement is achieved by Adaptive Grid Refinement in Fortran (AGRIF) [*Debreu et al*., 2008]. The applied "two-way nesting" approach allows for communication between the global model and the nest in both directions, i.e., on the one hand, the global base model provides the boundary conditions for the nest and on the other hand, the high-resolution nest feeds back the dynamics occurring in the nest onto the global model.

The more realistic representation of the complex Pacific Ocean bathymetry in this eddy-resolving model renders a better resolved ocean circulation, including western boundary currents and their extensions (see section 3 and Figure 2). The model's complex ITF pathways and correlation with ENSO have been examined by *van Sebille et al*. [2014]. Their study shows that TROPAC01 produces ITF transport and the mean and variability of Indo-Pacific sea surface height with good fidelity.

3. ENSO Winds and OGCM Experiments

The southward shift of wind anomalies during El Niño events can be readily described by the first two EOF modes of tropical Pacific zonal and meridional wind stress anomaly fields [*McGregor et al*., 2013]. To be consistent with the earlier study of *Kug et al*. [2003], we use N34 time series and the spatial pattern of the zonal

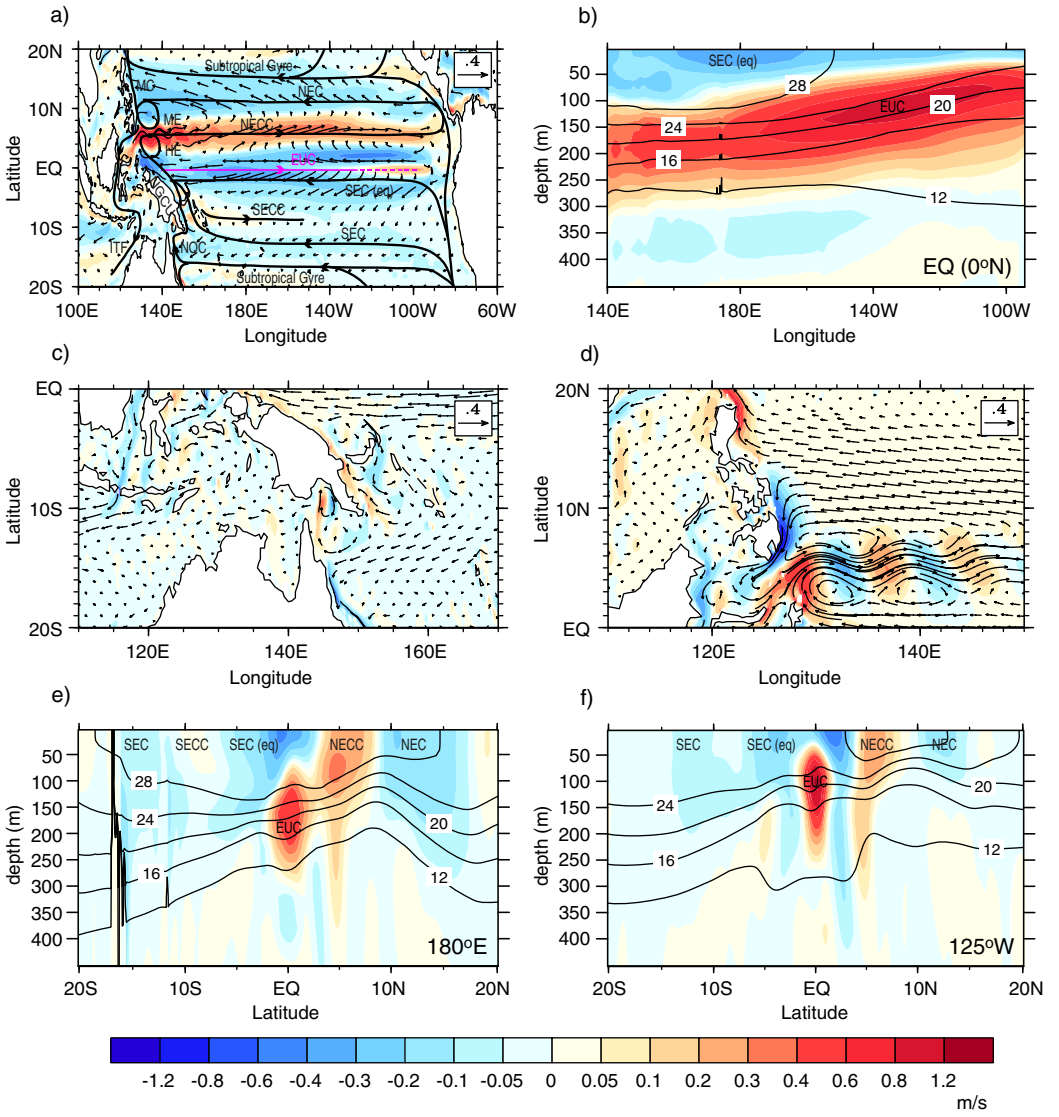

Figure 2. (a) Model mean surface (averaged over the upper 50 m) currents (m/s, vectors), with the zonal currents shaded. Overlaying this is a schematic representation of the Pacific's major ocean currents (black: surface, magenta: subsurface) of *Sen Gupta et al.* [2012]. (b) Zonal section of mean temperature (black contours) and zonal current (shaded) along the equator (m/s). (c, d) The model mean surface (averaged over the upper 50 m) currents (vectors), with the meridional currents shaded, zoomed in on the south-west and north-west equatorial Pacific regions, respectively. (e, f) Meridional sections of mean temperature (black contours) and zonal current (color shading, where red is eastward and blue westward; m/s) at the longitudes listed in the lower right corner of each figure. All of the major currents: North Equatorial Current (NEC), Mindanao Current (MC), North Equatorial Counter Current (NECC), Mindanao Eddy (ME), Halmahera Eddy (HE), Equatorial Under Current (EUC), South Equatorial Current (SEC), South Equatorial Counter Current (SECC), and Indonesian Through Flow (ITF) are labeled.

and meridional components of the ERA-interim wind stress anomalies regressed onto N34 to represent the pattern and time evolution of the first EOF (Figures 1a and 1c). These patterns of regression coefficients are virtually identical to those of the first EOF of equatorial wind stress anomalies, which accounts for 23% of the variance, with spatial correlations of 0.92 and 0.92 for the zonal and meridional components, respectively. The N34 index is also highly correlated with the corresponding principal component time series (correlation coefficient of 0.76), despite being somewhat smoother temporally.

These wind components, which are linearly related to ENSO, are then removed from the zonal and meridional wind stress anomaly time series at each spatial location, and the first EOF of the residual wind stress anomalies between 10°N–10°S and 100°E–60°W is then calculated. As discussed in section 1, this EOF, which accounts for 17% of the variance of the residual wind stress anomalies in the region, has been shown to be nonlinearly related to ENSO [*Stuecker et al.*, 2013]. The corresponding full Pacific domain spatial

pattern is then obtained by regressing the resulting principal component time series (Figure 1c) onto the residual wind stress anomalies at each spatial location (Figure 1b). The regressed wind stress patterns show meridionally asymmetric wind anomalies that are consistent with the second EOF of ERA-interim wind stress anomalies, with spatial correlations of 0.99 and 0.99 for the zonal and meridional components, respectively, and the corresponding principle component time series have a correlation of 0.997 with each other. As the spatial structure of these wind stress anomalies are highly asymmetric about the equator, these are hereafter referred to as the ENSO asymmetric wind stress anomalies (τ_{asym}). The wind anomalies that are linearly related to ENSO, on the other hand, are relatively symmetric about the equator in comparison and are thus referred to as the ENSO symmetric wind stress anomalies (τ_{sym}), as in *McGregor et al*. [2013].

Four experiments and one control simulation are then conducted with the high-resolution TROPAC01 OGCM, all of which span the period 1979–2007. Each of these simulations was branched off a 40 year spin-up control simulation forced with ERA-interim long-term monthly mean wind stress anomalies. The four experiments are exactly parallel to those done by *McGregor et al*. [2012a], which used a reduced gravity linear shallow water model. Experiment 1 (EXP_{SYM}) has time varying τ_{sym} added to the control simulation. Similarly, the second experiment (EXP_{ASYM}) has time varying τ_{asym} added to the control, while the third experiment (EXP_{BOTH}) has the wind stress anomalies reconstructed from both τ_{sym} and τ_{asym} added to the control. The fourth experiment is forced with the full ERA-interim wind stress anomalies (hereafter titled EXP_{FULL}). We note that as monthly mean wind stresses were utilized here, oceanic variance generated by wind stresses with shorter time scales is not simulated. The anomalous response of each experiment is calculated by removing the long-term monthly mean of the concomitantly extended control simulation.

Analysis of the control simulation reveals that TROPAC01 produces all of the major branches of the tropical Pacific surface circulation (Figure 2a). The realistic representation of western boundary coastal bathymetry and current paths in the southern and northern regions is displayed in Figures 2c and 2d. The former highlights the path of ITF and flows within the Coral Sea, both of which are consistent with observations [*Kessler and Cravatte*, 2013, Figure 13; *Sprintall et al*., 2009]. The latter highlights the path of the Mindanao current, the location of the Mindanao (ME), and Halmahera eddies (HE), along with the meanders of the North Equatorial Counter Current (NECC), all of which are consistent with observations from the region [*Kashino et al*., 2013, Figure 1]. Comparing with the observed subsurface current data of *Johnson et al*. [2002, Figure 2], we find that the control TROPAC01 simulation also accurately captures the location and strength of many subsurface currents, such as the Equatorial Under Current (EUC), the North Equatorial Counter Current (NECC), and the South Equatorial Current (SEC) (Figures 2b, 2e, and 2f).

4. Results

Meridional transports are calculated by vertically integrating the transport above the 16°C isotherm, which is taken to represent the lower thermocline (Figure 2). The Northern Hemisphere (NH) and Southern Hemisphere (SH) components of the zonally integrated meridional transport are calculated across the width of the Pacific Ocean, while ITF is calculated by integrating transports between New Guinea and Kalimantan. In order to focus on the interannual variations of the meridional transport, we removed the mean seasonal cycle and smoothed the resulting anomalous time series with a 5 month running mean prior to analysis and plotting.

Here we define the equatorial region as between 5°N and 5°S, consistent with the study of *Meinen and McPhaden* [2000]. Changes in WWV result from convergent and divergent meridional transports above 16°C at 5°N (V_{5N}) and 5°S (V_{5S}). WWV changes would occur most prominently when the meridional transport difference ($V_{5S} - V_{5N}$) is large, that is, when NH transports are in the opposite direction and of similar magnitude to SH transport. Consistent with expectations, WWV changes defined by the meridional transports above the 16°C isotherm are equivalent to the time derivative of the volume of water above the 16°C isotherm ($r = 0.81$). On the other hand, a nonzero value of the meridional transport average ($(V_{5N} + V_{5S})/2$) depicts a net upper ocean interhemispheric exchange. This is most likely to occur when the meridional transport in the NH is in the same direction as that of the SH. In an idealized situation, when the NH and SH transports are of similar magnitude and in the same direction, changes in WWV would be minimal as the amount entering the equatorial region at the 5°S, leaves the equatorial region at 5°N. However, as what we view as an interhemispheric exchange may also occur due to the unequal partitioning of transports north

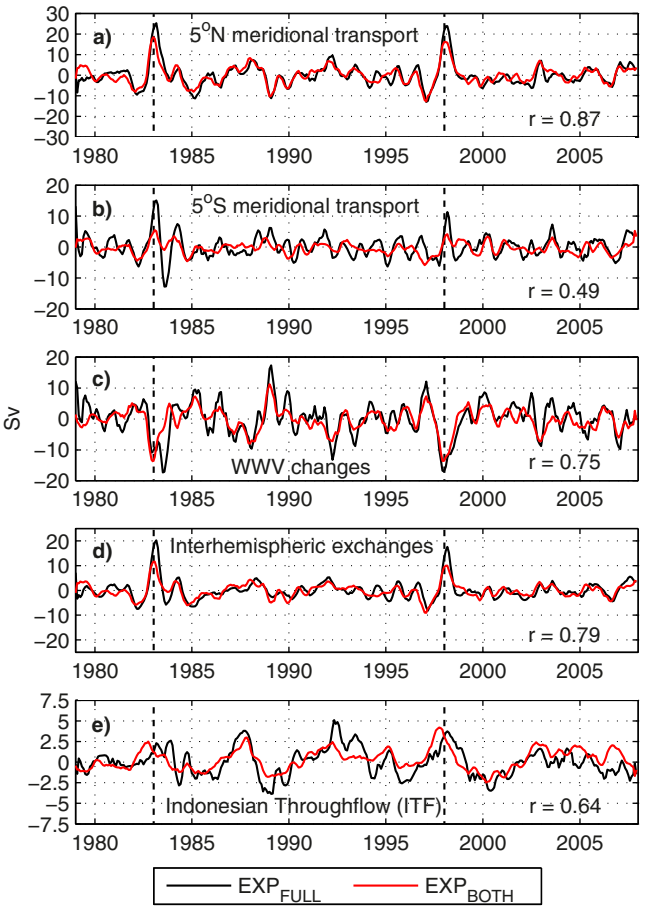

Figure 3. Pacific Ocean meridional transport (Sv) calculated at (a) 5°N and (b) 5°S, while WWV changes, interhemispheric exchanges, and ITF (calculated between New Guinea and Borneo) are, respectively, displayed in Figures 3c–3e. Transports from the EXP_{FULL} and EXP_{BOTH} are presented by black and red lines, respectively, in each figure. The two dashed vertical black lines represent the December to January peak of the 1982/1983 and 1997/1998 El Niño events. Correlation coefficients calculated between the figures displayed time series are presented in the bottom right corner.

and south of the equator, we compare the meridional average transport ($(V_{5N} + V_{5S})/2$) of EXP_{FULL} with the experiments meridional transports on the equator. We find a high correlation ($r = 0.97$) between the two transports that is statistically significant above the 99% level, indicating that the meridional average transport is indeed representative of interhemispheric exchanges. Note, the statistical significance coefficients determined in this study take account of serial (auto)correlation in the series based on the reduced effective number of degrees of freedom outlined by *Davis* [1976].

Comparing the meridional transports at 5°N from EXP_{BOTH} with those of EXP_{FULL} reveals that the EXP_{BOTH} simulation captures much of the EXP_{FULL} transport variability ($r = 0.87$; Figure 3a). At 5°S, on the other hand, EXP_{BOTH} only does a reasonable job in reproducing the EXP_{FULL} transport variability, as marked by a relatively weak correlation ($r = 0.49$) and underestimated transport magnitudes (Figure 3b). This suggests that there are processes other than τ_{sym} and τ_{asym} wind stresses that influence transport along 5°S. However, given the prominence of NH transports in the WWV and interhemispheric exchanges, EXP_{BOTH} captures much of the changes in WWV ($r = 0.75$) and interhemispheric exchanges ($r = 0.79$) seen in EXP_{FULL} (Figures 3c and 3d). EXP_{BOTH} also produces the ITF variability of EXP_{FULL} reasonably well ($r = 0.64$; Figure 3e). It is noteworthy that EXP_{BOTH} underestimates the magnitude of the interhemispheric exchanges of EXP_{FULL} during the large El Nino events by about 50% (Figure 3d). However, for a more straightforward interpretation, we compare the results of EXP_{SYM} and EXP_{ASYM} simulation with that of EXP_{BOTH} to determine the role of τ_{sym} and τ_{asym} in these changes. Note that the main conclusions of this manuscript do not change if we instead use EXP_{FULL} for comparison, with only slight reduction in the correlation coefficients.

Figure 4 shows the zonal mean meridional transports at 5°N and 5°S from EXP_{SYM} and EXP_{ASYM}, revealing a few interesting differences. For instance, in EXP_{SYM}, as a result of the symmetric wind stress pattern (τ_{sym}), the NH transports are positively correlated ($r = 0.69$) with the forcing time series (Figure 1c), while the SH transports are negatively correlated ($r = -0.39$). The magnitude of both correlations increases when the forcing time series leads the meridional transport. The NH maximum correlation ($r = 0.79$) occurs when this lead is 2 months, while the SH maximum absolute correlation ($r = -0.66$) when this lead is 3 months. The meridional transports lagging the forcing time series by a few months is consistent with the recharge oscillator, indicating that these transports are reliant on ocean dynamical adjustment.

In EXP_{ASYM}, on the other hand, the SH and NH transports are both positively correlated (0.79 and 0.76, respectively) with the forcing time series (τ_{asym}), and the maximum correlation occurs at zero lag (Figure 4b). This zero lag indicates that the meridional transports changes are likely a direct response to the wind

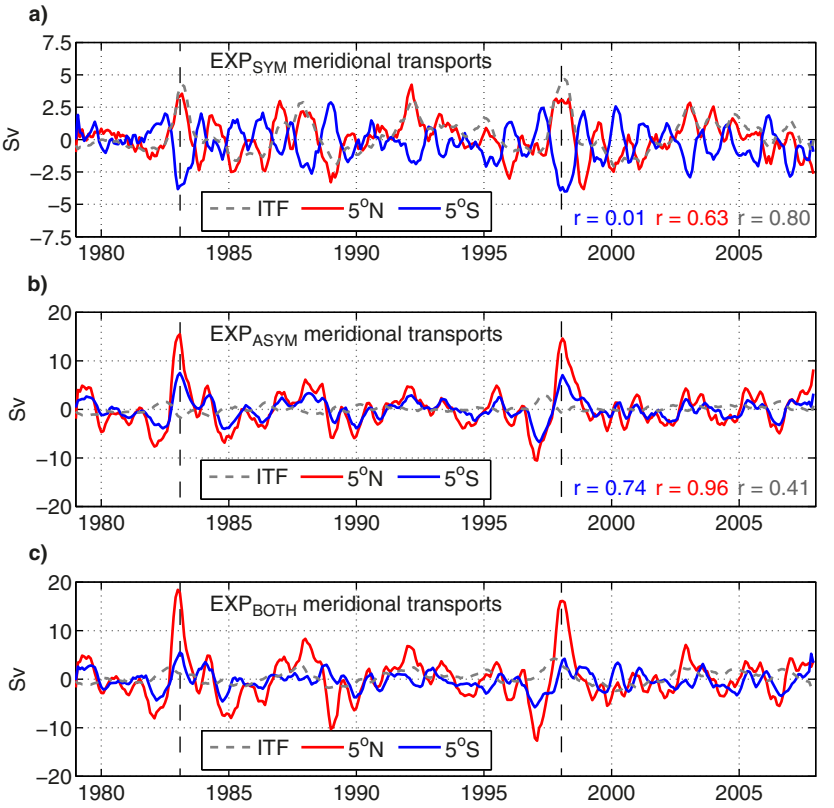

Figure 4. Pacific Ocean meridional transport (Sv) between New Guinea and Kalimantan at 2°S (hereafter titled ITF) and calculated at 5°N, and 5°S (see legend) calculated from the (a) EXP_{SYM}, (b) EXP_{ASYM}, and (c) EXP_{BOTH} simulations. The two dashed vertical black lines represent the December to January peak of the 1982/1983 and 1997/1998 El Niño events. Correlation coefficients calculated between the EXP_{SYM} and EXP_{ASYM} time series and those of EXP_{BOTH} are presented in the corresponding figures bottom right corner.

forcing. In fact, the Ekman transport calculated at 5°S displays a correlation of 0.76 when compared with the actual modeled transports of EXP_{ASYM}, and a correlation of 0.74 for 5°N (Figure 5).

Further differences between the meridional transports of these two experiments are highlighted in Figure 6, which shows the correlation of the meridional transport at any given latitude against the meridional transports at all other latitudes from the same experiment. These plots reveal that for EXP_{SYM}, the SH transports generally oppose the NH transports for all latitudes within 20° latitude of the equator (Figure 6a). This indicates that, neglecting the effect of ITF, which will be discussed in section 4.3, the EXP_{SYM} transports will in effect lead to changes in the equatorial region WWV. For EXP_{ASYM} on the other hand, transports as far south as 10°S are positively correlated with transports up to 15°N (Figure 6b). Thus, the NH and SH transports in EXP_{ASYM} are generally headed in the same direction, which implies that they will likely lead to significant interhemispheric exchanges. This is generally consistent with the study of *Kug et al.* [2003] who suggested that it is meridional asymmetries in the wind stress anomalies, in terms of the structure around the equator, which largely lead to interhemispheric exchanges.

Interestingly, at 5°N, the EXP_{SYM} meridional transports are positively correlated ($r = 0.48$) with the Ekman induced EXP_{ASYM} meridional transports. This means that both EXP_{SYM} and EXP_{ASYM} produce northward (southward) meridional transports during an El Niño (La Niña) events, which results in a larger magnitude of the NH transport variability in EXP_{BOTH} (Figure 4c). At 5°S, on the other hand, the EXP_{SYM} and EXP_{ASYM} transports are negatively correlated ($r = -0.54$). Thus, during an El Niño event, for instance, the northward transports of EXP_{ASYM} are partially offset by the southward transports of EXP_{SYM}. This destructive interference results in a more damped SH transport variability in EXP_{BOTH} relative to that in the NH (Figure 4c). However, as EXP_{SYM} only partially cancels the EXP_{ASYM} SH transports, the EXP_{BOTH} transport at 5°S largely tracks the EXP_{ASYM} transports. This is implied in the cross-latitudes correlations of EXP_{BOTH} (Figure 6c), where the transports between 0°S and 10°S generally display a positive correlation with the transports between 0°N and 10°N. This same feature is also apparent in the EXP_{FULL} correlations (Figure 6d); however, the correlations

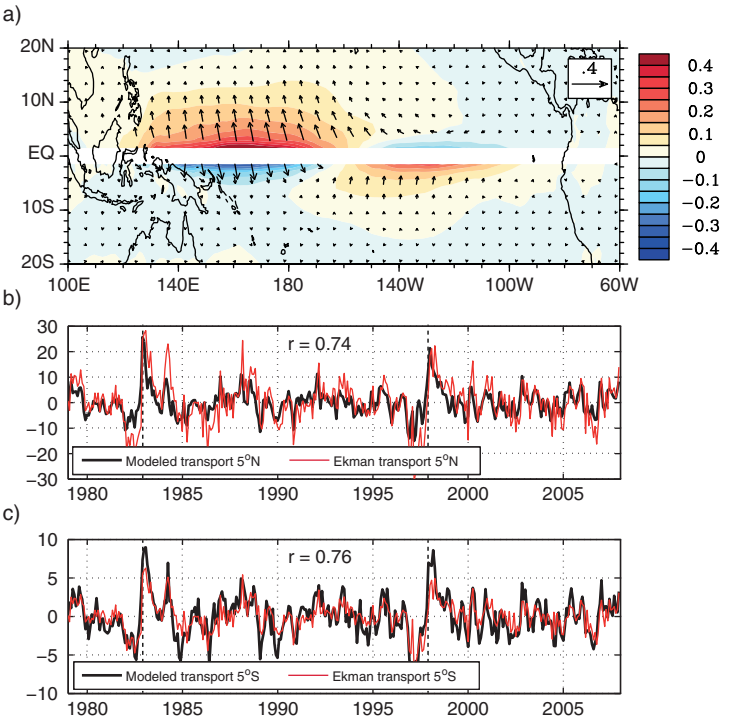

Figure 5. (a) The Ekman transport (vectors) of the spatial pattern of τ_{asym} (cf. Figure 1b), while the underlying shading displays the meridional component Ekman transport (Sv). The modeled EXP_{ASYM} and τ_{asym} calculated Ekman transports (Sv) calculated across 5°N and 5°S are presented in Figures 5b and 5c, respectively.

are not as prominent as they are for EXP_{BOTH}, as expected since EXP_{FULL} contains higher-order processes not captured by EXP_{BOTH}.

4.1. Warm Water Volume Changes

We find that WWV changes of EXP_{SYM} (Figure 7a) are largely consistent with the classic linear view of the Recharge Oscillator paradigm of *Jin* [1997]. That is, during an El Niño (La Niña) event the τ_{sym} wind stress anomalies create an eastward (westward) tilt of the tropical thermocline (Figure 8a) and an Ekman-driven equatorward (poleward) surface transport (Figure 8b). The tilted thermocline in turn creates a meridional geostrophic transport, which causes an anomalous subsurface mass divergence (convergence) about the equator (Figure 8c). Thus, the Ekman and geostrophic transports due to τ_{sym} are opposing transports that largely occur away from the ocean boundaries (Figures 8b and 8c). The western boundary transports in both hemispheres also generally oppose the interior geostrophic transports (Figure 8a). It is noted, however, that the subsurface meridional geostrophic transport is larger than the surface Ekman transport and the western boundary currents combined. This results in a net mass divergence (convergence) near the equator during El Niño (La Niña) events (Figures 7a and 8a).

We also find that the total transport in each hemisphere can be largely reproduced by combining the western boundary and interior WWV changes only ($r_{NH} = 0.89$, $r_{SH} = 0.88$). This indicates that the eastern boundary flows play little role in the total transport and WWV discharge consistent with earlier studies [e.g., *Kug et al.*, 2003].

Focusing now on the equatorial WWV changes of EXP_{ASYM} (Figure 7a), we find that these WWV changes are correlated with the EXP_{ASYM} (τ_{asym}) forcing time series at zero lag ($r = -0.75$, significant at the 95% level). This is consistent with the dominant role of Ekman transport in the 5°S and 5°N total transports (Figure 5). The fact that EXP_{ASYM} produces WWV changes appears to contrast the fact that both the NH and SH transports of this experiment are highly correlated (correlation coefficient of $r = 0.91$ between meridional transport at 5°S and 5°N), which implies these transports should largely lead to interhemispheric exchanges. However, it is the differences in the magnitude of these correlated Ekman-induced transports that lead to these changes in WWV in EXP_{ASYM}. For instance, the northward transport at and after the peak of the extreme 1982/1983 and 1997/1998 El Niño events is much larger in the NH than the SH, which ultimately leads to an equatorial region divergence and a related decrease in WWV (Figure 4b).

In regards to what role τ_{sym} (EXP_{SYM}) and τ_{asym} (EXP_{ASYM}) play in the EXP_{BOTH} equatorial WWV changes (Figure 8a), both appear to play a roughly equal role. Both experiments produce WWV changes that are highly correlated with the EXP_{BOTH} WWV changes (Figure 8a), while also having comparable magnitudes. In fact, the addition of EXP_{ASYM} in EXP_{BOTH} can be viewed to double the variance of EXP_{SYM}-induced WWV changes, in accordance with the shallow water model results of *McGregor et al.* [2012a].

Thus far, the WWV changes have been predetermined to be confined within 5°S and 5°N, that is, the latitudinal extent that defines the equatorial region. Here we consider variations to this latitudinal extent, which

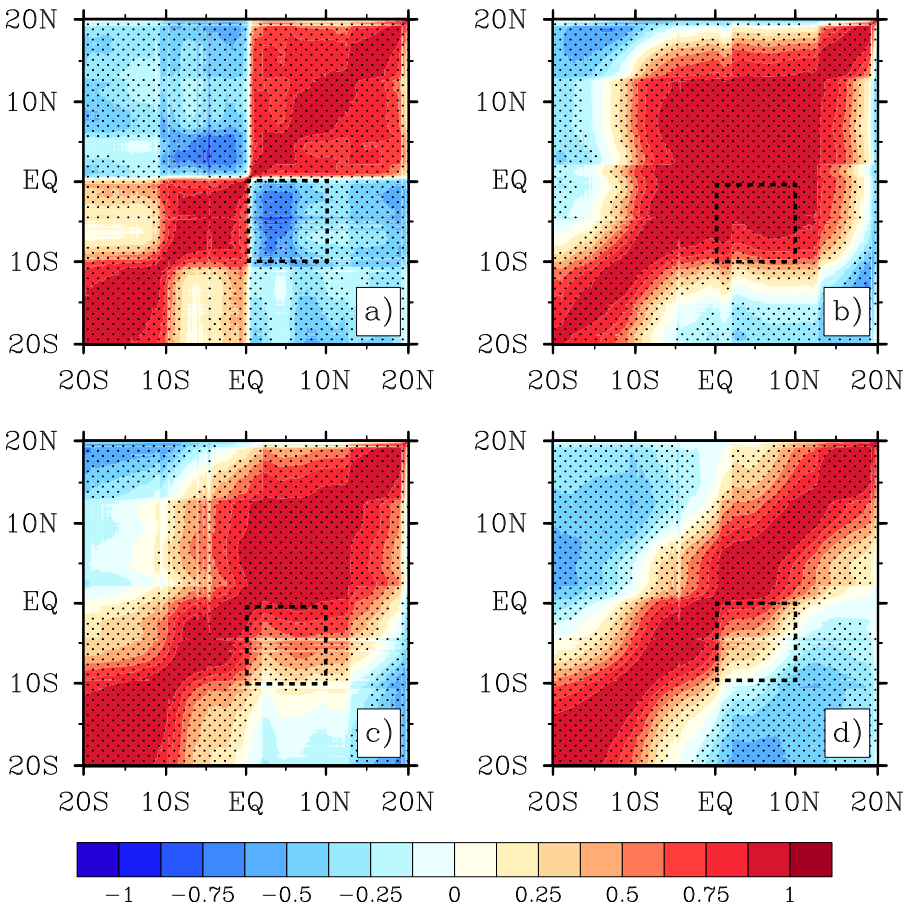

Figure 6. Correlation coefficients calculated between the meridional transports of the (a) EXP_{SYM}, (b) EXP_{ASYM}, (c) EXP_{BOTH}, and (d) EXP_{FULL} simulations at any given latitude with all other latitudes from the same experiment. Statistically significant (>95%) correlation coefficients are denoted by stippling. The dashed box region in each figure simply highlights the correlation between transports at 0°S–10°S and those at 0°N–10°N.

will allow us to examine whether the τ_{sym} and τ_{asym} wind forcings allow for more effective exchanges between the equator and higher latitudes. Figure 7b shows variance of WWV change as a function of latitudinal extent (i.e., between 1°N–1°S, 2°N–2°S, . . ., 20°N–20°S). First, this plot demonstrates that the maximum WWV change in EXP_{BOTH} occurs when the equatorial region boundary is set at 5°S–5°N, thus confirming these latitudes as the most appropriate location that defines the equatorial region in terms of mass exchange. However, once decomposed into τ_{sym} and τ_{asym}, a clear difference emerges: EXP_{SYM} shows that the effective mass exchange occurs closer toward the equator (about 3°–5°). On the other hand, this is mass exchange is occurring farther poleward in EXP_{ASYM} (about 7°–12°). The implication of this difference will be discussed in section 5.

4.2. Interhemispheric Exchanges

In EXP_{BOTH} upper ocean mass is transferred from the NH to the SH in the lead up to an El Niño event. This interhemispheric exchange then abruptly switches sign just prior to the event peak leading to a SH to NH exchange (Figure 9a). These SH to NH exchanges are the largest during the strongest El Nino events of 1982/1983 and 1997/1998, in the order of 10 Sv.

The interhemispheric transports of EXP_{SYM} are clearly much smaller than those of EXP_{BOTH} and have virtually zero correlation (Figure 9a). This result is somewhat contradictory to the role of τ_{sym} forcing in the interhemispheric exchanges as reported by *Kug et al*. [2003]. One of the reasons for this disagreement is likely due to the fact that the *Kug et al*. [2003] study only considered interior transports. We find that the interior transports (i.e., transports away from the eastern and western continental boundary) at 5°N in EXP_{SYM} are significantly larger than that occurring at 5°S (Figure 8a), consistent with *Kug et al*. [2003]. However, on average

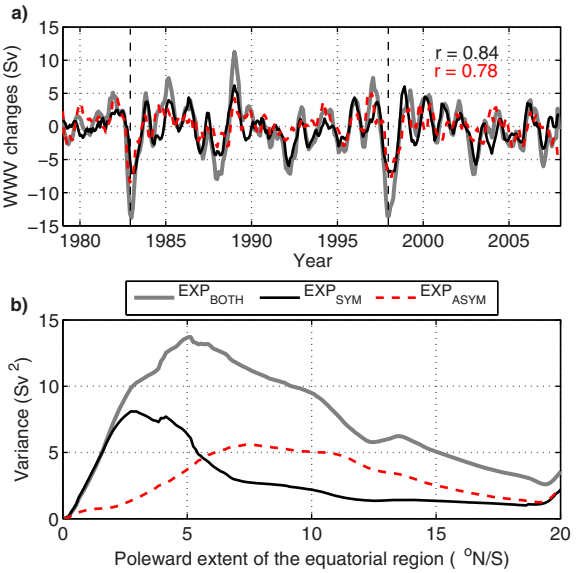

Figure 7. (a) WWV changes (Sv), defined as the transport at 5°S minus the transport at 5°N, from EXP_{SYM} (black), EXP_{ASYM} (dashed red), and EXP_{BOTH} (gray). The two dashed vertical black lines represent the December to January peak of the 1982/1983 and 1997/1998 El Niño events, while the black (red) correlation (r) value is the correlation between EXP_{SYM} (EXP_{ASYM}) WWV and the WWV of EXP_{BOTH}. (b) The variance of WWV changes (Sv^2) from EXP_{SYM} (black), EXP_{ASYM} (dashed red), and EXP_{BOTH} (gray), where the latitudes defined to encompass the equatorial region are varying symetrically and displayed on the *x* axis.

this strong asymmetry in interior transport is largely, though not completely, compensated by the western boundary transports (i.e., the boundary transports at the given latitude generally oppose the interior transport at that latitude), thus making its overall impact relatively small. Note, western (eastern) boundary transports are defined here as transports occurring between the continental boundary and 10° longitude offshore.

On the other hand, EXP_{ASYM} reproduces the majority of the EXP_{BOTH} interhemispheric exchanges (Figure 9a). This is reflected by the correlation coefficient of 0.98 calculated between the EXP_{ASYM}-induced interhemispheric exchanges and those of the EXP_{BOTH}. The role of EXP_{ASYM} is not surprising given the anomalous transports at 5°N and 5°S are in the same direction in both hemispheres (Figures 4 and 10).

As expected, due to the fact that the EXP_{ASYM} meridional transports are largely Ekman-induced, the EXP_{ASYM} interhemispheric exchanges are largely confined to the upper 50 m (Figures 10b and 10c) and are significantly (above the 95% level) correlated with the τ_{asym} forcing time series at zero lag ($r = 0.73$). Thus, these results indicate that EXP_{ASYM} forcing (τ_{asym}) is largely responsible for the hemispheric exchanges in EXP_{BOTH}, while EXP_{SYM} forcing (τ_{sym}) plays a negligible role. Thus, the dominant role of τ_{asym} in these exchanges explains why their amplitude appears to be related to ENSO intensity, while the phase appears related to the annual cycle [*Stuecker et al*., 2013].

As the meridional movement of τ_{asym} wind stress anomalies is shown to increase with increasing El Niño amplitude, while remaining relatively small regardless of La Niña amplitude [*McGregor et al*., 2013], we expect the interhemispheric exchanges during large El Niño events to be stronger than those occurring during La Niña events. That is, we expect the discharge of warm water during an El Niño event to be asymmetric about the equator and the asymmetry to be more prominent with increasing event magnitude, while the recharge of heat during La Niña events should be much more symmetric. Indeed, composites of interhemispheric exchanges (i.e., the asymmetric component of the meridional transport) during El Niño events and those during La Niña events (Figures 9b and 9c) show that this is the case. Note that in Figure 9c the interhemispheric exchanges have been normalized by the maximum magnitude of the ENSO event (N34 SSTA). These normalized transports show that the interhemispheric exchanges that occur during extreme El Niño events are approximately twice as large as those occurring during La Niña events. Similar asymmetries are found in the EXP_{FULL} (not shown).

4.3. Indonesian Throughflow (ITF)

Up until now we have not considered the ITF in our calculations of WWV or interhemispheric exchanges. As noted in section 2, ITF is calculated around 2°S by integrating transports between New Guinea and Kalimantan. ITF was purposefully neglected as to focus on the Sverdrup component of the ENSO WWV changes. However, as these interbasin exchanges have the potential to alter WWV, their effects need to be considered. Here, changes in WWV are now defined as the difference between the transport at 5°S,

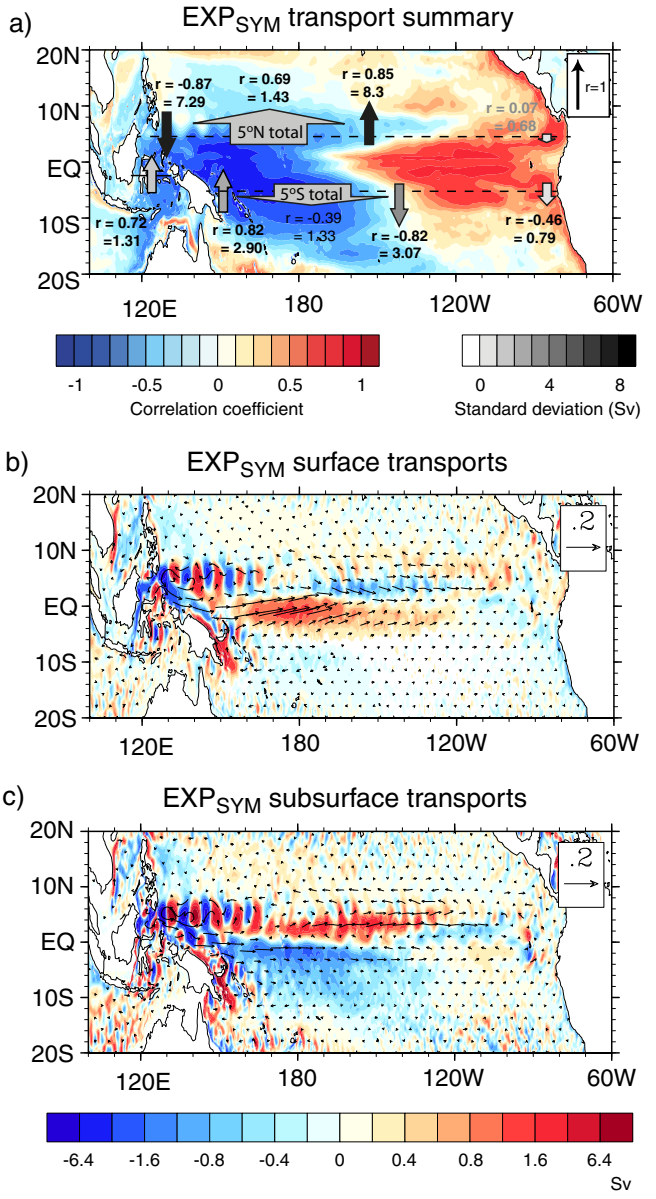

Figure 8. (a) Schematic illustration of the meridional transports into and out of the equatorial region during EXP_{SYM}. Vector length coresponds to the size of the correlation cofficient calculated between the wind stress forcing time series and the transport. Note that the thick vectors represent the integrated basin wide transport, while the thin vectors represent the transports in each section (western boundary, interior and eastern boundary). The color of all vectors coresponds to the standard deviation of the meridional transport. Note, the numbers above (below) each vector in the NH (SH) are the correlation coefficient (upper number) and standard deviation (lower number) of the meridional transport (Sv) at that location. Numbers that are black (gray) indicated correlations that are (not) statistically significant above the 95% level. Background shading indicates the correlation coefficient calculated between the wind stress forcing time series and the depth of the 16°C isotherm. (b) The regression coefficients calculated between the EXP_{SYM} forcing time series and the meridional transport in the upper 50 m (shading) and the regression coefficients calculated between the EXP_{SYM} forcing time series and the average currents in the upper 50 m (vectors). (c) As in Figure 8b except for the transports and currents below 50 m and above the 16°C isotherm.

including the ITF, and 5°N $[(V_{5S} + V_{ITF}) - V_{5N}]$, while interhemispheric exchanges are defined as the average of the transport at 5°N and the transport at 5°S with ITF transport added $[(V_{5N} + V_{5S} + V_{ITF})/2]$.

The ITF is driven by the strong pressure gradient between the two basins, whereby the dynamic height of the western Pacific Ocean is significantly higher than that of the eastern Indian Ocean. Thus, changes in this gradient, through variations in dynamical height in the western Pacific or eastern Indian Ocean regions, will lead to changes in the ITF. Such changes can be driven by large-scale modes of variability, such as ENSO and the Indian Ocean Dipole (IOD) [*Sprintall and Revelard*, 2014]. For instance, the lower (higher) SSH in the western equatorial Pacific during El Niño (La Niña) events leads to weakened ITF that taken alone would lead to an anomalous increase (decrease) in WWV [see *van Sebille et al.*, 2014, and references therein]. Given that our simulations are purposefully forced only with wind stress anomalies related to ENSO (Figure 3c), we do not capture the full variability of the ITF. Nevertheless, these simulations allow us to identify how ITF responds to ENSO and to put this in the context of WWV changes and the recharge oscillator framework.

First, breaking down the role of EXP_{SYM} and EXP_{ASYM} in the ITF of EXP_{BOTH}, we find that EXP_{SYM} plays the dominant role in these changes ($r = 0.81$; Figure 11). The dominance of EXP_{SYM} is due the wind forcing more directly modulating the interbasin pressure gradient via the related east-west thermocline tilt (Figure 8a). The ITF of EXP_{ASYM} plays a relatively minor role as there is a relatively small western Pacific thermocline depth signal (Figure 10a), thus the transports are significantly smaller and less correlated ($r = 0.41$) with EXP_{BOTH} ITF at zero lag. It is interesting to note, however, that the EXP_{ASYM} ITF leads the EXP_{BOTH} ITF by several months. This is a result of upper ocean mass being transferred from the NH to the SH prior to the El Niño event peak which results

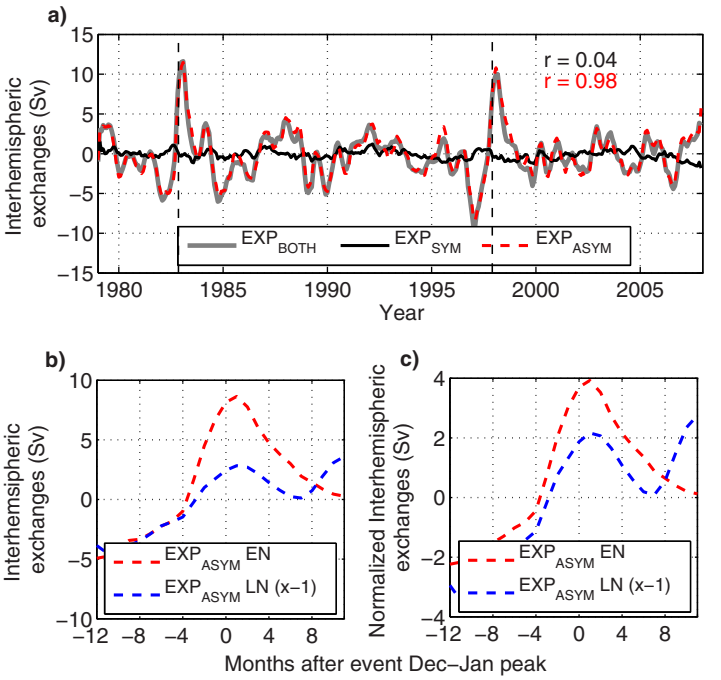

Figure 9. (a) Interhemispheric exchanges (Sv, positive = northward), defined as the average of the transport at 5°S plus the transport at 5°N, from EXP_{SYM} (black), EXP_{ASYM} (dashed red), and EXP_{BOTH} (gray). The two dashed vertical black lines represent the December to January peak of the 1982/1983 and 1997/1998 El Niño events, while the black (red) correlation (r) value is the correlation between EXP_{SYM} (EXP_{ASYM}) interhemispheric exchanges and the exchanges of EXP_{BOTH}. (b) The El Niño (La Niña x-1) EXP_{ASYM} interhemispheric exchange composite mean. (c) As in Figure 9b, but the interhemispheric exchanges have been normalized by dividing by the maximum absolute value of ENSO (N34 SSTA) at the event DJF peak.

in lower than normal sea level showing up in the NH first, consistent with the sea level study of *Widlansky et al.* [2014].

Focusing on EXP_{SYM} in order to understand the role of ITF in the traditional recharge oscillator framework, we find that the ITF is highly correlated with the forcing time series (0.72) and this correlation increases to 0.9 when the forcing time series leads ITF by 2–3 months. This positive correlation, which is consistent with our theoretical understanding, indicates that this Indian Ocean leakage contributes to an increase (decrease) in WWV while at the same time it is being discharged (recharged) during El Niño (La Niña) through Sverdrup transport across 5°S and 5°N in the Pacific. The large contribution of EXP_{SYM} in the ITF variability is apparent in Figure 4a. For instance, during a typical El Niño event, the EXP_{SYM} ITF is increasing equatorial WWV at a similar rate to the decrease in WWV due to transports across either the northern or southern boundary of the equatorial region. A similar damping effect is seen during La Niña events, but a nonlinearity in the ITF (not shown) means it is a little bit less apparent. The damping by the ITF on WWV changes is corroborated by the fact that taking the ITF into account in the calculations of EXP_{SYM} WWV roughly halves the variance of the changes without dramatically changing the temporal evolution (Figure 12a).

While the EXP_{SYM} WWV variability decreases due to the addition of the ITF, the interhemispheric exchanges of EXP_{SYM} can be viewed to increase if the ITF is considered part of either the NH or SH transport. There are reasons that ITF should be classified as both: because on the one hand the ITF is calculated along 2°S (SH) and on the other, the upper ocean water is largely sourced from the NH [e.g., *van Sebille et al.*, 2014]. Regardless, the overall impact on the interhemispheric exchanges is consistent. That is, it can be seen to either cancel out the SH transports or enhance the NH transports. Either way, including ITF into the calculations of EXP_{SYM} WWV leads to an increased mass transfer from SH to NH during El Niño events, and this exchange is approximately mirrored during La Niña events (Figure 12b).

In summary, the inclusion of ITF acts to damp WWV changes and amplify the interhemispheric exchanges when looking through the classic view of the recharge oscillator as represented by EXP_{SYM}. However, when viewed from the more complete picture of WWV changes and interhemispheric exchanges in EXP_{BOTH}, the role of the ITF is less apparent. First, as the addition of τ_{asym} acts to amplify the EXP_{BOTH} WWV changes (i.e., by enhancing the discharge of WWV during El Niño events and vice versa for La Niña events), adding the ITF into calculations of WWV of EXP_{BOTH} has only a relatively small damping effects (figure not shown). Second, as the interhemispheric exchanges of EXP_{BOTH} are largely due to τ_{asym}, the increased magnitudes of EXP_{SYM} interhemispheric exchanges due to ITF has only little effect (not shown).

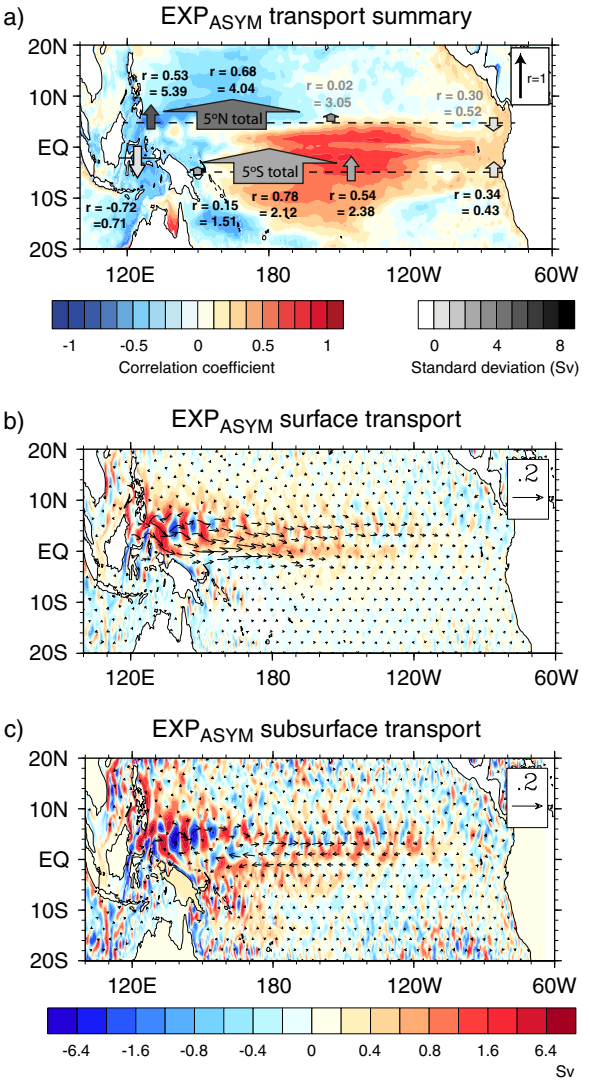

Figure 10. As in Figure 8, but for EXP$_{ASYM}$.

5. Summary and Conclusions

We identify the meridionally quasi-symmetric (τ_{sym}) and asymmetric (τ_{asym}) wind stress anomalies related to ENSO in the ERA-interim reanalysis product (Figure 1) and use a series of high-resolution OGCM experiments to examine their relative impact on WWV changes and interhemispheric exchanges during ENSO events. It is noted that this study implicitly assumes linearity in the experiment design ($EXP_{SYM} + EXP_{ASYM} = EXP_{BOTH}$) and analysis (i.e., breaking the transports down into their various components), and despite the results being largely consistent with linear theory, nonlinearities may play some role in the modeled and observed meridional transports.

τ_{sym} is the classic ENSO wind stress response, identified by simply linearly regressing ENSO SSTA against surface wind stress anomalies. On the other hand, τ_{asym}, identified by an EOF analysis, is largely dominated by a Philippine Sea anticyclone-type structure [*Wang et al*., 1999] in the Northern Hemisphere and a westerly wind stress anomalies in the Southern Hemisphere. *Stuecker et al*. [2013] have shown τ_{asym} to be a physically meaningful mode that owes its existence to the nonlinear atmospheric response to the annual cycle and ENSO SSTs combined. As discussed in *McGregor et al*. [2012a, 2013], the linear combination of τ_{sym} and τ_{asym} describes most of the ENSO wind stress anomalies. These anomalies, which are largely symmetric about the equator prior to the ENSO event peak, shift southward around boreal winter event peak [e.g., *Harrison*, 1987; *Harrison and Vecchi*, 1999].

The high-resolution OGCM was utilized to give a more realistic representation of the circulation in and around the complex bathymetry of the western Pacific. The model output reveals how complex the transports are along the northern boundary of the equatorial region (5°N, Figure 13a). This northern boundary, which is dynamically defined (Figure 7b), bisects the latitudinally narrow eastward flowing North Equatorial Counter Current (NECC). Thus, the meanders of the NECC and the eddy activities along this zonal boundary make the spatial variability of the meridional transports large (Figure 13a) in comparison to what is seen at 5°S (Figure 13b). The location of this variability is consistent with the location of eddies observed in altimeter data [*Chelton et al*., 2011]. While the zonally integrated flow is generally consistent with expectations, these highly variable small-scale structures do emerge in any composite or regression analysis (Figures 8b, 8c, 10b, 10c, and 13). Thus, this raises the importance of an adequately resolved observational network.

τ_{sym} forcing (EXP_{SYM}) generates an oceanic response that is largely consistent with the classic linear view of the Recharge Oscillator paradigm of *Jin* [1997]. During an El Niño event, the τ_{sym} wind anomalies create an anomalous Sverdrup transport (section 4.1), which discharges upper ocean mass from the equatorial region (Figure 8).

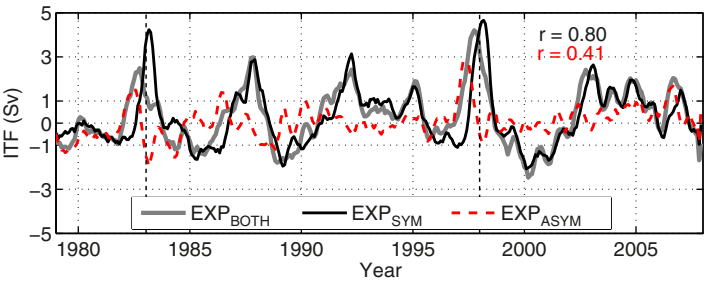

Figure 11. Indonesian Throughflow (ITF) transport (Sv), defined as the transport calculated around 2°S by integrating transports between New Guinea and Kalimantan at 2°S, from EXP_{SYM} (black), EXP_{ASYM} (dashed red), and EXP_{BOTH} (gray). The two dashed vertical black lines represent the December to January peak of the 1982/1983 and 1997/1998 El Niño events, while the black (red) correlation (r) value is the correlation between EXP_{SYM} (EXP_{ASYM}) ITF and the ITF of EXP_{BOTH}.

La Niña events largely mirror the changes seen during El Niño events. We also find that the associated WWV changes, at least in the idealized OGCM simulation presented here (EXP_{SYM}), are considerably damped by the ITF transport (Figure 12a). That is, as the WWV is decreasing during an El Niño event, due to the divergence of mass away from the equatorial region, the ITF weakens and thus anomalously transports mass back into the equatorial region (Figure 11). The converse largely occurs during La Niña events (Figure 11); however, the magnitude is not so large, as there appears to be an ENSO phase nonlinearity in the magnitude of the ITF. The direction of anomalous ITF transports is consistent with theoretical expectations [*Wyrtki*, 1987; *Clarke and Liu*, 1994]. The damping of the WWV changes by the ITF in turn acts to more than double the magnitude of the interhemispheric exchanges (Figure 11b). As the ITF can be viewed to either amplify the transport at 5°N, or damp the transport 5°S, it creates a larger difference between the NH and SH transports, and thus increasing the interhemispheric exchanges.

τ_{asym} forcing (EXP_{ASYM}), on the other hand, predominantly generates surface Ekman transport (cf. Figures 5 and 10). This Ekman transport is generally of the same sign over the entire basin, and in the lead up to an El Niño event it generates large-scale southward surface flow over much of the tropical Pacific. As a result of changes in the annual cycle phase [*Stuecker et al.*, 2013], this flow abruptly changes sign just prior to the event peak, leading to large-scale northward flow over much of the basin (Figures 5b and 5c).

Our series of experiments reveal that τ_{asym} forcing is largely responsible for the Pacific Ocean's interhemispheric exchanges. This result appears somewhat consistent with the findings of *Kug et al.* [2003], as it is wind stress anomalies that are asymmetric about the equator which generate these interhemispheric exchanges and that these exchanges are largely related to Ekman transports. The main differences between the results presented here and those of *Kug et al.* [2003] are derived from the fact that τ_{asym} forcing was not considered by *Kug et al.* [2003]. This result also provides a dynamical understanding of the Pacific Ocean interhemispheric sea level seesaw reported by *Widlansky et al.* [2014]. We also find an ENSO phase asymmetry in these interhemispheric exchanges, whereby the interhemispheric exchanges that occur during extreme El Niño events are approximately twice as large as those occurring during La Niña events. That is, the recharge of heat during a large

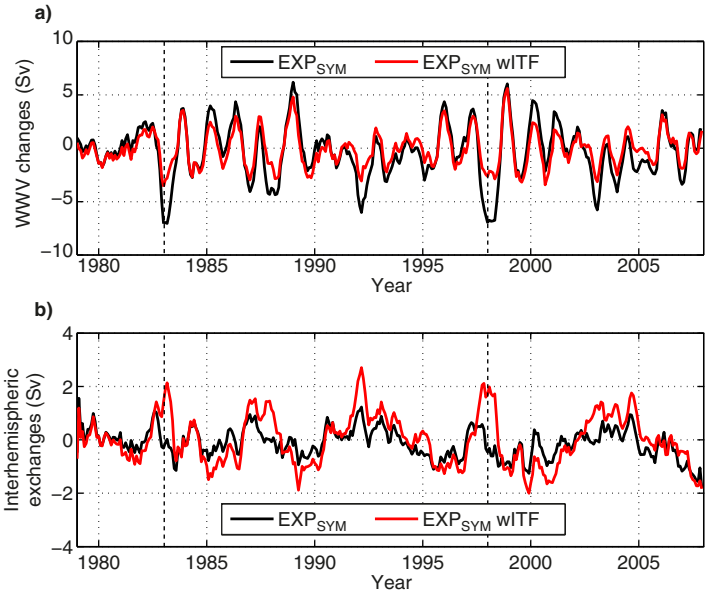

Figure 12. Role of ITF in EXP_{SYM} (a) WWV changes, and (b) interhemispheric exchanges. The black lines in both figures do not include ITF in the calculations, while the red lines do. The two dashed vertical black lines represent the December to January peak of the 1982/1983 and 1997/1998 El Niño events.

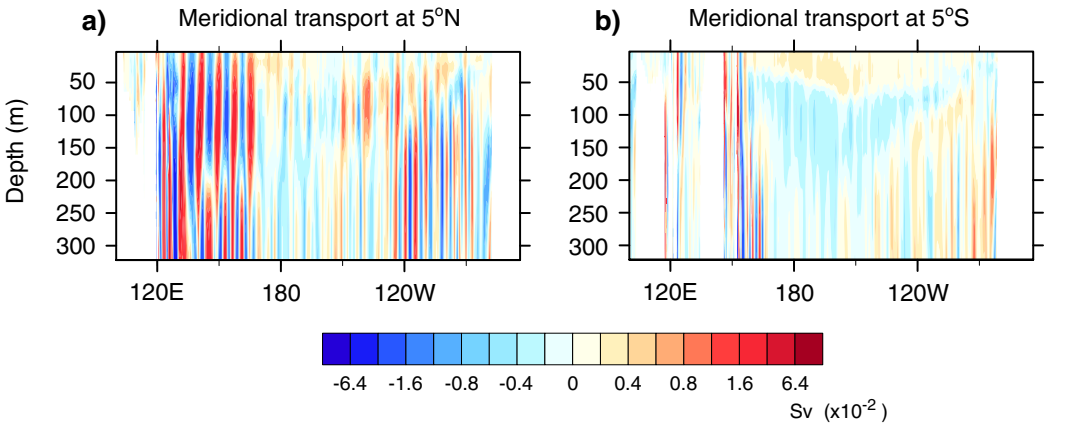

Figure 13. The November to March average large El Niño event (1982/1983, 1991/1992, 1997/1998) composite mean meridional transports (Sv $\times$ 10^{-2}) from EXP_{BOTH} at (a) 5°N and (b) 5°S.

La Niña event appears to be more symmetric about the equator than the discharge of heat during a large El Niño event.

As τ_{asym} forcing (EXP_{ASYM}) generates transports that are largest north of the equator in the western tropical Pacific (Figures 5 and 10), during periods of southward flow these transports converge in the equatorial region leading to increases in WWV (i.e., in the lead up to an El Niño event). During periods of northward flow (i.e., around the peak of an El Niño event), on the other hand, the transports diverge in the equatorial region and leading to a decrease in equatorial region WWV. Thus, these EXP_{ASYM}-induced meridional transports directly alter equatorial WWV and play a crucial role in the discharging process, as documented in *McGregor et al*. [2012a] using a shallow water model. In fact, approximately half of the changes in equatorial region WWV are due to τ_{asym} forcing, which makes τ_{asym} forcing a vital component of ENSO. It is interesting to also note that the timing of the τ_{asym} forced WWV changes is roughly consistent with those expected of the recharge oscillator paradigm, which makes it easy to confuse the total WWV changes with our conceptual view of the recharge oscillator.

As discussed in section 1, most of the meridional mass transports into or out of the Pacific equatorial region are known to occur at its northern boundary [*Kug et al*., 2003]. Combining the results of τ_{sym} and τ_{asym} forcing, as was done in EXP_{BOTH}, goes a long way in reproducing this observational feature (Figures 3 and 4). Our results show that this is largely due to the fact that the NH meridional transport forced by τ_{asym} constructively interferes with the NH meridional transport of τ_{sym}, while the SH transport of τ_{asym} destructively interferes with the SH meridional transport of τ_{sym}. For instance, during large El Niño events, τ_{asym} produces northward transports that are predominantly constrained to the surface (Figure 14b), while the τ_{sym}

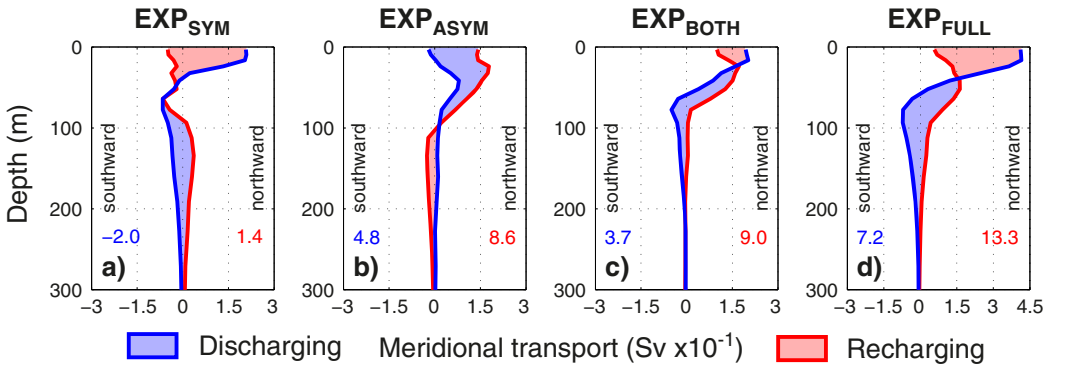

Figure 14. Large El Niño event (1982/1983, 1991/1992, 1997/1998) composite mean meridional transports from (a) EXP_{SYM}, (b) EXP_{ASYM}, (c) EXP_{BOTH}, and (d) EXP_{FULL} integrated across 5°N (red lines) and 5°S (blue lines). The shaded blue and red regions, respectively, indicate the discharging and recharging effects of the transport on the equatorial region WWV, while the inset numbers indicate the vertical integral of the composite mean integrated meridional transport.

produces southward surface transports and northward subsurface transports (Figure 14a). Combined, these two forcings produce northward transport over the entire water column as the northward surface transports of τ_{asym} overpower the southward transports of τ_{sym} (Figures 14c and 14d). In regards to the SH meridional transports during large El Niño events, τ_{asym} again produces northward transports that are predominantly constrained to the surface (Figure 14b), while τ_{sym} produces northward surface transports and southward subsurface transports (Figure 14a). The combined northward surface transports are large enough during these events that they overcompensate the subsurface southward transport (Figures 14c and 14d). Thus, the meridional transport of forced by τ_{asym} acts to amplify the NH transports at the same time as damping the SH transports, thereby creating the north-south asymmetry in the magnitude of the net meridional transports seen in the observations. Our results also suggest that the asymmetric effects of τ_{asym} are not as pronounced during small El Niño events and even less so during La Niña events (Figure 9), implying that these events are more consistent with that expected from the recharge oscillator theory [*Jin*, 1997].

Perhaps the most important potential implication of the results presented here is the fact that τ_{asym} appears to be largely responsible for linking ENSO with the off-equatorial regions. That is, the equatorial WWV and interhemispheric exchanges associated with the classic ENSO wind stress response (τ_{sym}), identified by simply linearly regressing ENSO SSTA against surface wind stress anomalies, is largely confined to between $\pm 5^{\circ}$ latitude (Figure 7b). It is the forcing associated with τ_{asym} that appears to link ENSO to the off-equatorial region (Figure 7b). This is of importance because numerous studies have suggested that the equatorial and off-equatorial oceans are linked at decadal time scales [e.g., *Kleeman et al*., 1999], and these links may be responsible for the Pacific Ocean's decadal variability. For instance, the coupled General Circulation Model study of *McGregor et al*. [2009] suggested that ENSO behavior could be modulated by wind stress forced off-equatorial ocean perturbations. The results of this study suggest that ENSO itself, through τ_{asym} forcing, can create an off-equatorial signal that may then feed back in the equatorial region and modulate ENSO behavior.

Acknowledgments

The TROPAC01 experiment output analyzed in this paper, which exceeds 3TB when compressed, is stored at the University of New South Wales long-term data store. This data will be made available on request to the corresponding author. The model integrations were performed at the North-German Supercomputing Alliance (HLRN). We gratefully acknowledge the support of the DRAKKAR group in the model development. This work was supported by the Australian Research Council (ARC) including the ARC Centre of Excellence in Climate System Science. This is PMEL contribution 4203.

References

Alory, G., and T. Delcroix (2002), Interannual sea level changes and associated mass transports in the tropical Pacific from TOPEX/Poseidon data and linear model results (1964–1999), *J. Geophys. Res.*, *107*(C10), 3153, doi:10.1029/2001JC001067.

Arakawa, A., and V. R. Lamb (1977), Computational design of the basic dynamical processes of the UCLA general circulation model, in *Methods of Computational Physics*, vol. 17, pp. 173–265, Academic, N. Y.

Cai, W., G. Meyers, and G. Shi (2005), Transmission of ENSO signal to the Indian Ocean, *Geophys. Res. Lett.*, *32*, L05616. doi:10.1029/2004GL021736.

Chang, P., et al. (2006), Climate fluctuations of tropical coupled systems—The role of ocean dynamics, *J. Clim.*, *19*, 5122–5174.

Chelton, D. B., M. G. Schlax, and R. M. Samelson (2011), Global observations of nonlinear mesoscale eddies, *Prog. Oceanogr.*, *91*, 167–216, doi:10.1016/j.pocean.2011.01.002.

Clarke, A. J., and X. Liu (1994), Interannual sea level in the northern and eastern Indian Ocean, *J. Phys. Oceanogr.*, *24*, 1224–1235.

Davis, R. E., (1976), Predictability of sea surface temperature and sea level pressure anomalies over the North Pacific Ocean, *J. Phys. Oceanogr.*, *6*, 249–266.

Debreu, L., C. Vouland, and E. Blayo (2008), AGRIF: Adaptive grid refinement in Fortran, *Comput. Geosci.*, *34*, 8–13.

Dee, D. P., and S. P. Uppala (2009), Variational bias correction of satellite radiance data in the ERA-Interim reanalysis, *Q. J. R. Meteorol. Soc.*, *135*, 1830–1841.

Harrison, D. E. (1987), Monthly mean island surface winds in the central tropical Pacific and El Niño events, *Mon. Weather Rev.*, *115*, 3133–3145.

Harrison, D. E., and G. A. Vecchi (1999), On the termination of El Niño, *Geophys. Res. Lett.*, *26*, 1593–1596.

Johnson, G. C., B. M. Sloyan, W. S. Kessler and K. E. McTaggart (2002), Direct measurements of upper ocean currents and water properties across the tropical Pacific Ocean during the 1990's, *Prog. Oceanogr.*, *52(1)*, 31–61.

Jin, F.-F. (1997), An equatorial ocean recharge paradigm for ENSO. Part I: Conceptual model, *J. Atmos. Sci.*, *54*, 811–829.

Kashino, Y., A. Atmadipoera, Y. Kuroda, and Lukijanto (2013), Observed features of the Halmahera and Mindanao Eddies, *J. Geophys. Res. Oceans*, *118*, 6543–6560, doi:10.1002/2013JC009207.

Kessler, W. S., and S. Cravatte (2013), Mean circulation of the Coral Sea, *J. Geophys. Res. Oceans*, *118*, 6385–6410, doi:10.1002/2013JC009117.

Kleeman, R., J. P. McCreary, and B. A. Klinger (1999), A mechanism for the decadal variation of ENSO, *Geophys. Res. Lett.*, *26*, 1743.

Kug, J.-S., I.-S. Kang, and S.-I. An (2003), Symmetric and antisymmetric mass exchanges between the equatorial and off-equatorial Pacific associated with ENSO, *J. Geophys. Res.*, *108*(C8), 3284, doi:10.1029/2002JC001671.

Madec, G. (2008), *NEMO Ocean Engine—Version 3.1, Note du Pole de Modélisation*, Inst. Pierre-Simon Laplace (IPSL), No. 27, France.

McGregor, S., A. S. Gupta, N. J. Holbrook, and S. B. Power (2009), The modulation of ENSO variability in CCSM3 by extratropical Rossby waves, *J. Clim.*, *22*, 5839–5853, doi:10.1175/2009JCLI2922.1.

McGregor, S., A. Timmermann, N. Schneider, M. F. Stuecker, and M. H. England (2012a), The effect of the South Pacific convergence zone on the termination of El Niño events and the meridional asymmetry of ENSO, *J. Clim.*, *25*, 5566–5586, doi:10.1175/JCLI-D-11-00332.1.

McGregor, S., A. S. Gupta, and M. H. England (2012b), Constraining wind stress products with sea surface height observations and implications for Pacific Ocean sea level trend attribution, *J. Clim.*, *25*, 8164–8176, doi:10.1175/JCLI-D-12–00105.1.

McGregor, S., N. Ramesh, P. Spence, M. H. England, M. J. McPhaden, and A. Santoso (2013), Meridional movement of wind anomalies during ENSO events and their role in event termination, *Geophys. Res. Lett.*, *40*, 749–754, doi:10.1002/grl.50136.

McPhaden, M. J., S. E. Zebiak, and M. H. Glantz (2006), ENSO as an integrating concept in earth science, *Science*, *314*, 1740–1745, doi:10.1126/science.1132588.

Meinen, C. S., and M. J. McPhaden (2000), Observations of warm water volume changes in the equatorial Pacific and their relationship to El Niño and La Niña, *J. Clim.*, *13*, 3551–3559.

Meinen, C. S., and M. J. McPhaden (2001), Interannual variability in warm water volume transports in the equatorial Pacific during 1993–1999, *J. Phys. Oceanogr*, *31*, 1324–1345.

Okumura, Y. M., and C. Deser (2010), Asymmetry in the duration of El Niño and La Niña, *J. Climate*, *23*, 5826–5843.

Sen Gupta, A., A. Ganachaud, S. McGregor, J. N. Brown, and L. Muir (2012), Drivers of the projected changes to the Pacific Ocean equatorial circulation, *Geophys. Res. Lett.*, *39*, L09605, doi:10.1029/2012GL051447.

Smith, T. M., R. W. Reynolds, T. C. Peterson, and J. Lawrimore (2008), Improvements to NOAA's historical merged land-ocean surface temperature analysis (1880–2006), *J. Clim.*, *21*, 2283–2296.

Sprintall, J., and A. Revelard (2014), The Indonesian Throughflow: Response to Indo-Pacific climate variability, *J. Geophys. Res.*, *119*, 1161–1175, doi:10.1002/2013JC009533.

Sprintall, J., S. E. Wijffels, R. Molcard, and I. Jaya (2009), Direct estimates of the Indonesian Throughflow entering the Indian Ocean: 2004–2006, *J. Geophys. Res.*, *114*, C07001, doi:10.1029/2008JC005257.

Stuecker, M. F., A. Timmermann, F.-F. Jin, S. McGregor, and H.-L. Ren (2013), A combination mode of annual cycle and the El Niño/Southern Oscillation, *Nat. Geosci.*, *6*, 540–544, doi:10.1038/ngeo1826.

van Sebille, E., J. Sprintall, F. U. Schwarzkopf, A. S. Gupta, A. Santoso, M. H. England, A. Biastoch, and C. W. Boning (2014), Pacific-to-Indian Ocean connectivity: Tasman leakage, Indonesian Throughflow, and the role of ENSO, *J. Geophys. Res. Oceans*, *119*, 1365–1382, doi:10.1002/2013JC009525.

Wang, B., R. Wu, and R. Lukas (1999), Roles of the western North Pacific wind variation in thermocline adjustment and ENSO phase transition, *J. Meteorol. Soc. Jpn.*, *77*, 1–16.

Widlansky, M. J., A. Timmermann, S. McGregor, M. F. Stuecker, and W. Cai (2014), An interhemispheric tropical sea level seesaw due to El Niño Taimasa, *J. Clim.*, *27*, 1070–1081, doi:10.1175/JCLI-D-13-00276.1.

Wyrtki, C. (1987), Indonesian through flow and the associated pressure gradient, *J. Geophys. Res.*, *92*, 12,941–12,946.